

# Water Resources Research



## RESEARCH ARTICLE

10.1029/2019WR025563

## Intraseasonal Drainage Network Dynamics in a Headwater Catchment of the Italian Alps

N. Durighetto<sup>1</sup> , F. Vingiani<sup>1</sup> , L. E. Bertassello<sup>2</sup> , M. Camporese<sup>1</sup> , and G. Botter<sup>1</sup> 

<sup>1</sup>Department of Civil, Environmental and Architectural Engineering, University of Padua, Padua, Italy, <sup>2</sup>Lyles School of Civil Engineering, Purdue University, West Lafayette, IN, USA

### Key Points:

- We present the results of a high-resolution survey of drainage network dynamics in the Alps
- Most of the observed streams are dynamical, and spatial patterns of drainage density are driven by geologic heterogeneity
- The temporal dynamics of the active stream length are controlled by both short-term and long-term antecedent rainfall

### Supporting Information:

- Supporting Information S1

### Correspondence to:

N. Durighetto,  
nicola.durighetto@phd.unipd.it

### Citation:

Durighetto, N., Vingiani, F., Bertassello, L. E., Camporese, M., & Botter, G. (2020). Intraseasonal drainage network dynamics in a headwater catchment of the Italian Alps. *Water Resources Research*, 56, e2019WR025563. <https://doi.org/10.1029/2019WR025563>

Received 14 MAY 2019

Accepted 19 MAR 2020

Accepted article online 23 MAR 2020

**Abstract** In the majority of existing studies, streams are conceived as static objects that occupy predefined regions of the landscape. However, empirical observations suggest that stream networks are systematically and ubiquitously featured by significant expansion/retraction dynamics produced by hydrologic and climatic variability. This contribution presents novel empirical data about the active drainage network dynamics of a 5 km<sup>2</sup> headwater catchment in the Italian Alps. The stream network has been extensively monitored with a biweekly temporal resolution during a field campaign conducted from July to November 2018. Our results reveal that, in spite of the wet climate typical of the study area, more than 70% of the observed river network is temporary, with a significant presence of disconnected reaches during wet periods. Available observations have been used to develop a set of simple statistical models that were able to properly reconstruct the dynamics of the active stream length as a function of antecedent precipitation. The models suggest that rainfall timing and intensity represent major controls on the stream network length, while evapotranspiration has a minor effect on the observed intraseasonal changes of drainage density. Our results also indicate the presence of multiple network expansion and retraction cycles that simultaneously operate at different time scales, in response to distinct hydrological processes. Furthermore, we found that observed spatial patterns of network dynamics and unchanneled lengths are related to the underlying heterogeneity of geological attributes. The study offers novel insights on the physical mechanisms driving stream network dynamics in low-order alpine catchments.

## 1. Introduction

Empirical evidence shows unambiguously that stream networks are highly dynamic and respond to changing climatic conditions over a multitude of time scales that range from single events to annual (and even longer) periods (Costigan et al., 2016). However, river networks are assumed to be static objects in the majority of existing hydrological, ecologic, and biogeochemical studies (e.g., Cardenas, 2007; Ceola et al., 2014; Gatto et al., 2013; Muneeppeerakul et al., 2008; Raymond et al., 2013).

The shape and length of river networks are fundamental for a number of different biological and chemical processes, including ecological dispersion (Berger et al., 2017; Muneeppeerakul et al., 2008; Tonkin et al., 2017) and in-stream nutrient cycling (e.g., Bernal & Sabater, 2008; Butturini et al., 2008; Datry, Fritz & Leigh, 2016; Bertuzzo et al., 2017; Wiginton et al., 2005). River networks, particularly in headwaters, represent the active linkage among geosphere, hydrosphere, and atmosphere. Consequently, intermittence in the presence of flowing water strongly impacts nutrient availability, processing, and transport. In this context, particular emphasis (e.g., Boodoo et al., 2017; Raymond et al., 2013) has been given by the scientific community and the general public to carbon dioxide emissions associated to stream outgassing.

The study of the response of stream intermittency to unsteady climatic forcing is a major challenge for improving our understanding of river networks form and function. These temporal changes in the spatial configuration of river networks have long been recognized by hydrologists (Anderson & Burt, 1978; Blyth & Rodda, 1973; Day, 1978; Gregory & Walling, 1968; Gregory & Gardiner, 1979; Hewlett & Nutter, 1970; Morgan, 1972; Roberts, 1978; Roberts & Klingeman, 1972; Tischendorf, 1969, as noted by Godsey & Kirchner, 2014). More recently, the topic has generated a renewed interest in the scientific community. These late efforts have been devoted to better describe and understand the spatiotemporal dynamics of stream networks under a variety of climatic settings (Costigan et al., 2015; Floriancic et al., 2018; Jaeger et al., 2007; Jensen et al., 2017; Jaeger et al., 2019; Jensen et al., 2019; Godsey & Kirchner, 2014; Goulsbra et al.,

©2020. The Authors.

This is an open access article under the terms of the Creative Commons Attribution-NonCommercial License, which permits use, distribution and reproduction in any medium, provided the original work is properly cited and is not used for commercial purposes.

2014; Lovill et al., 2018; Shaw, 2016; Shaw et al., 2017; Peirce & Lindsay, 2015; Ward et al., 2018; Wiginton et al., 2005; Whiting & Godsey, 2016; Zimmer & McGlynn, 2017). In most cases, however, either the spatial scale or the temporal resolution of existing observational studies has been limited by the huge practical burden typically associated to stream network mapping by visual inspection (but see Jensen et al., 2019; Peirce & Lindsay, 2015). Therefore, most of the available experimental datasets on river network dynamics do not exceed 2 km<sup>2</sup>/month. As a result, some research is still needed to fully understand the drivers of event-based stream dynamics in relatively large catchments (>1 km<sup>2</sup>), where empirical data could contribute to identifying scaling laws of network dynamics and emergent patterns of stream persistency.

A limited number of studies about river network dynamics have been conducted in continental Europe so far, and only few of them provided a full survey of the flowing stream network on a regular basis. In some cases, the analysis was restricted to individual stretches (Doering et al., 2007; Medici et al., 2008) or to the channel heads only (Agren et al., 2015), not including the full geometrical complexity of the river network and the presence of disconnected reaches. Other studies, instead, monitored the hydrologic status of a predefined set of nodes that do not necessarily correspond to the entire network (Datry, Fritz & Leigh 2016), leading to a possible underestimation of the drainage density. In other cases, sporadic surveys were performed (van Meerveld et al., 2019) preventing a full characterization of the stream network variability over multiple time-scales. To the best of our knowledge, Malard et al. (2006) is the only study where regular surveys of the whole active network were conducted in the continental Europe. However, their study catchment is relatively small (0.67 km<sup>2</sup>) and the ecological implications of network dynamics were investigated with a limited view on the underlying hydrological drivers.

To elucidate the changes of the active stream network in response to wetting/drying cycles, recent studies linked the length of the flowing network to the streamflow at the catchment outlet using empirical power-law regressions (Jensen et al., 2018; Prancevic & Kirchner, 2019; Shaw et al., 2017; Ward et al., 2018). However, network length and streamflow dynamics can be seen as the joint response to common hydroclimatic processes, impacted by the meteorologic and physiographic features of the contributing catchment (Costigan et al., 2016). Accordingly, Shaw (2016) stated that “the timing of contraction of the active channel network did not correspond to the timing of streamflow recession. These two phenomena occur at much different scales, with recession occurring in a matter of days but channel contraction occurring over weeks and months.” For this reason, it would be insightful to explain the variability of the stream network length as a function of climatic variables.

Few studies have directly linked network dynamics to climatic variables such as antecedent precipitation and evapotranspiration (Blyth & Rodda, 1973; Goulsbra et al., 2014; Jaeger et al., 2019; Jensen et al., 2018, 2019; Morgan, 1972; Ward et al., 2018), but none of them allows the prediction of the stream network length based on precipitation data alone. Moreover, in all the existing studies the aggregation time scale of the precipitation input (or its range) was predefined. Consequently, the full spectrum of impacts of rainfall variability on stream length dynamics—and particularly the combined effects of short-term and long-term rainfall—has not been captured yet.

In this paper, we report and discuss the results of a biweekly field mapping of the stream network conducted in a relatively pristine headwater catchment of the Italian Alps. The spatial configuration of the stream network has been mapped nine times across the summer and early fall of 2018. This novel dataset achieves a noteworthy combination of duration of the field campaign (4 months), temporal resolution (about 2.5 surveys/month), areal coverage (>5 km<sup>2</sup> of contributing catchment), and spatial resolution (mapping streams down to 10 cm in width), allowing the study of network dynamics at different time scales and the investigation of the emergent spatial patterns of stream persistency. The collected data were utilized to inform a set of statistical models for the prediction of the length of the stream network based on simple climatic parameters. These models were compared to identify the relevant climatic variables that drive the dynamics of active network length and the temporal scales over which these dynamics take place. Additional analyses were then performed using the available morphometric and geologic data to explore the spatial heterogeneity of river network dynamics under different hydrological conditions.

The specific goals of this paper are the following: (i) to expand the geographic reach of research on the topic of temporary stream length through a biweekly dataset gathered in a 5.3 km<sup>2</sup> catchment of the Italian Alps; (ii) to identify the major meteorological variables that drove the temporal network dynamics across the summer and fall seasons of 2018; (iii) to identify the temporal scales over which the expansion/contraction

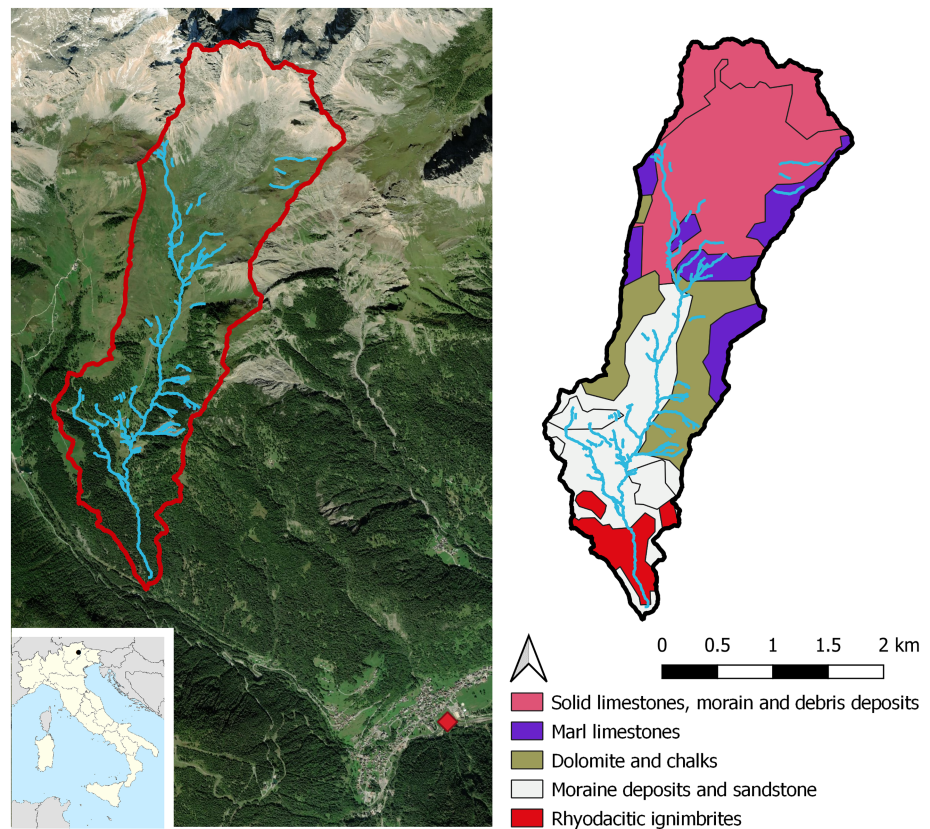


**Figure 1.** Left: orthophoto showing the different land covers of the Valfredda river catchment and its location in Italy. Catchment boundaries are depicted with an orange line; light blue lines represent the potential river network as surveyed; the red marker shows the position of the weather station. Right: geologic map of the area.

cycles of stream network take place; and (iv) to analyze the spatial heterogeneity of network dynamics across different geologic regions of the catchment.

The key research hypothesis is that climatic variables are the main drivers of temporal dynamics of the overall stream length, while storage dynamics and internal physiographic features (geology and land cover) dictate the frequencies and the spatial patterns of drainage network expansion/contraction cycles. Under this hypothesis, the role of the climatic forcing can be disentangled from that of other hydrological and physiographic characteristics of the catchment, thereby allowing the prediction of network length starting from climatic data. This provides important clues for the modeling of the network response to wetting and drying cycles. The additional research hypothesis is that the dynamics of flowing network length are the result of a superposition of multiple expansion/contraction cycles that reflect distinct flow generation mechanisms, which operate over different time scales. These hypotheses are tested by combining statistical analyses and formal model ranking with extensive experimental observations.

## 2. Material and Methods

### 2.1. Study Area and Climatic Data

The Rio Valfredda is a small alpine creek in northern Italy belonging to the Piave river basin (Figure 1, for more details on the basin the reader is referred to Botter et al., 2010; Lazzaro et al., 2013). The catchment elevation ranges from 1,500 to 3,000 m a.s.l., with a maximum drainage area of 5.3 km<sup>2</sup>. Lithology and vegetation cover exhibit significant spatial heterogeneity across elevations, shaping the hydrological dynamics of the basin. On the uplands, deposits of gravel and rocky debris, originated from the erosion of solid rock emergencies near the divides, dominate. These deposits are covered by shallow and patchy pastures that generate karst areas that ensure a high soil permeability, thereby promoting the infiltration of most part of the precipitation (as confirmed by the results of the field campaign). Below 2,400 m a.s.l., soil covers a sedimentary bedrock with trees growing adjacent to the streams. The lower part of the catchment (below 2,000

m a.s.l.) is characterized by an almost impermeable pyroclastic bedrock and a forested cover (as shown in Figure 1 and described in Section 3.3). There are several springs supplying aqueduct intakes, which collectively withdraw a flow rate that is two orders of magnitude smaller than the stream discharge at the outlet. Accordingly, the effects of these intakes on stream network dynamics were neglected.

The site has an alpine climate, characterized by high precipitation throughout the year (annual rainfall of about 1,500 mm), with significant snowfall during winter and melting in spring. The hydrological regime exhibits a strong seasonality, with winter low flows (when the whole catchment is covered by snow) followed by higher discharges during spring and summer. Because of low recession rates in winter and high rain frequency in the other seasons, intraseasonal flow regimes are mainly persistent (*sensu* Botter et al., 2013).

Climate data were monitored by a weather station of the Veneto Region Environmental Protection Agency (ARPAV) located in Falcade, 4.5 km far from the catchment centroid (Figure 1). These data are characterized by a daily resolution and are available since 2010. Monitored variables include precipitation, temperature, relative humidity, solar radiation, wind speed, and direction. These data were analyzed to characterize the climatic regime of the study catchment, especially during the field campaign (summer-fall 2018). Two additional weather stations were installed within the catchment area in 2019, after the completion of the field campaign described in this paper. Precipitation records gathered by these instruments were compared with the corresponding time series of the ARPAV weather station to ensure that the data used in this study represent sufficiently well the dynamics of the water input in the study catchment (see supporting information). The morphology of the Valfredda was characterized via a LiDAR survey that was carried out in October 2018 to produce a high-resolution (20 cm) digital terrain model (DTM) and a corresponding orthophoto.

## 2.2. Field Mapping of the Active Drainage Network

The drainage network was mapped nine times during a biweekly field campaign from July to early November 2018; the specific date of each survey was selected on the basis of the antecedent precipitation in order to maximize the variability of the observed conditions (Table 1). An additional survey was performed in January 2019, while the catchment was partly covered by snow. This survey was not used for modeling purposes but only to obtain an estimate of the extent of the drainage network during the winter time. The goal of the field campaign was to delineate the geometry of the potential drainage network (i.e., the maximum possible extent of the flowing network) and to map the presence of flowing water during each survey. The potential drainage network was identified by the presence of either flowing water during at least one survey or permanent channelization signs (e.g., absence of vegetation on a narrow strip of otherwise vegetated terrains and concave areas with clear continuous channel-like erosion pathways). The geometry of the network was specified by nodes (points) connected by stretches (continuous lines). A node was marked at every channel head (i.e., the upstream point of channelized or potentially channelized reaches), at every confluence point and approximately every 20 m between. The location of each node was dictated by local properties of the network, such as river meandering or the specific position of wet/dry and dry/wet transitions. Additional nodes were included to better describe the location of surface flow initiation/cessation during each survey. For this reason, the spatial resolution of the surveys is higher than the initial nodes spacing (20 m). Each node was coded as active when there was visible water flow with a minimum width of 10 cm, and dry otherwise. The above width threshold was selected because it was noted that below this threshold, the local microtopography might impact the status of each node by creating very unstable flow conditions in space and time (ponding/dry/wet) as a byproduct of extremely low flows (e.g., 1 L/min). This threshold is also consistent with the resolutions that can be typically achieved using remote imagery, such as thermal cameras installed on drones, whose use is planned in the upcoming months to improve the temporal resolution of the surveys. Each survey involved about eight people and lasted a single day. The survey consisted in walking the entire length of the drainage network, moving upstream along each tributary and collecting the GPS coordinates of network nodes with the aid of a geotracking device. In addition to mapping the network from the outlet upstream, the hillslopes were also scouted to ensure the mapping of channels that are disconnected from the outlet. The scouting was informed by vegetation greenness patterns derived from satellite imagery and by a reference network extracted from the DTM, with a very small threshold on the contributing area (0.5 ha). Nevertheless, all the hillslopes and areas far away from the connected network in the upper part of the basin were also monitored by hiking the whole catchment area to avoid under-representation of existing channels.



**Table 1**

Summary of the Field Surveys, With Total Rainfall in the 5 and 35 Days Prior to the Survey ( $h_5$  and  $h_{35}$ , Respectively), the Active Drainage Network Length (ADNL, in km and as a Percentage of the 16.2 km of Mapped Potential Drainage Network), the Active Drainage Density, the Disconnected ADNL (in km and %), and the Number of Disconnected Clusters (i.e., the Number of Active Stretches That Are Not Connected at the Surface to the Outlet)

Date	$h_5$	$h_{35}$	ADNL		Active drainage density	Disconnected ADNL		Disconnected clusters
	(mm)	(mm)	(km)	%	( $\text{km}^{-1}$ )	(km)	%	(-)
12 Jul 2018	27.6	157.4	9.16	56	1.72	1.70	10.5	31
26 Jul 2018	1.2	196.6	9.25	57	1.71	1.76	10.9	33
07 Aug 2018	25.0	225.6	10.36	64	1.95	2.29	14.1	36
23 Aug 2018	32.0	190.0	10.14	62	1.91	1.83	11.3	30
04 Sep 2018	49.4	257.8	11.28	69	2.13	3.30	20.4	41
13 Sep 2018	0.2	216.4	9.36	58	1.77	1.75	10.8	33
01 Oct 2018	12.2	124.4	7.97	49	1.50	1.17	7.2	18
26 Oct 2018	0.0	25.8	6.41	39	1.21	0.63	3.9	13
03 Nov 2018	54.2	347.8	12.48	77	2.35	3.45	21.3	49
18 Jan 2019	1.6	9.4	5.46	33	1.06	0.78	4.8	14

### 2.3. Network Delineation

Stream network maps were obtained combining information from field surveys and remotely sensed imagery, including the high-resolution DTM and the orthophoto. The DTM was aggregated to a resolution of 1 m to reduce the computational effort associated to its manipulation. The DTM was then preprocessed using a pit removal algorithm: A threshold of 300 m<sup>2</sup> was chosen on the basis of field observations to discriminate between real pits (not removed by the algorithm) and artifacts of the DTM that should be removed. Flow directions were then calculated using the D8 algorithm (Ocallaghan & Mark, 1984; Tarboton, 1996) and manually corrected in 132 pixels on the basis of field observations to properly represent local anomalies in the observed drainage network, due to human interventions (e.g., presence of roads and hiking trails). Finally, the contributing areas were calculated for each cell based on the corrected flow directions.

The coordinates of the field-collected nodes were adjusted by snapping the nodes over pixels of the DTM where accumulation of the contributing area occurs. Orthophotos were also used to ensure the correct positioning of each node. Maximum horizontal corrections were below 10 m, consistent with the positioning error of the system used for the field survey. The corrections applied to the flow directions and the adjustments on the coordinates of field-mapped nodes ensured that DTM-derived information and data from the field surveys were consistent with each other.

The drainage network was then delineated by connecting all the nodes with stream stretches, following flow directions along individual streams. Each stretch of the network was considered as active during a given survey only if both the upstream and downstream nodes were simultaneously active.

To quantify the dynamics of the stream network, a persistency index ( $P_i$ ) was calculated for each stretch ( $i$ ) dividing the number of times the stretch  $i$  was active by the total number of field surveys.  $P_i$  represents the percentage of surveys during which a stretch was active, and under the ergodic assumption, it provides an indication of the probability of that stretch being active during the campaign. The idea of quantifying the probability of network activity through spatial maps was first introduced by Jensen et al. (2017), even though in that case such probabilities were derived from the flow duration curve, whereas in this paper, maps of  $P_i$  were calculated directly from observational data. While still relying on the assumption that the available surveys properly represent the temporal variability of the status of each node, our method relaxes the additional hypothesis that a unique active network configuration exists for a given discharge at the outlet. Stretches with  $P_i = 1$  were classified as persistent, while stretches with  $0 < P_i < 1$  were coded as temporary; stretches with  $P_i = 0$  were indicated as dry, to underline the fact that they were inactive in all the field surveys. It must be noted that the value of  $P_i$  depends on the number/dates of field surveys conducted. Accordingly, a stretch classified as persistent (or dry) in this study may become temporary after the completion of additional field campaigns.

Five key properties of the drainage network were calculated for each field survey.

1. Active drainage network length (*ADNL* [km]): the total length of the active drainage network on a given date.
2. Active drainage density ( $\text{km}^{-1}$ ): *ADNL* divided by the catchment area.
3. Active disconnected drainage network length (disconnected *ADNL* [km]): length of the active drainage network that is not connected at the surface to the outlet.
4. Number of active channel heads: the number of origins of the active drainage network, hereafter named sources, including all the points in which surface flow resumes downstream of a disconnection along the potential network.
5. Disconnected clusters: the number of contiguous parts of the active network that are disconnected from the outlet.

The mean and variance of *ADNL* were also calculated, to be used as indicators of the mean drainage density and the extent of stream network dynamics.

#### 2.4. Spatial Patterns of Stream Network and Unchanneled Lengths

Local geologic features and heterogeneity of land cover may have a primary impact on the generation of the active stream network and the supply of surface flows, possibly giving rise to pronounced spatial heterogeneity in the observed drainage density. The heterogeneity of the bedrock properties and parental material in the catchment was analyzed using the Italian Geologic Map released online by the Italian Institute for Environmental Protection and Research (ISPRA). An extract of the map is reported in Figure 1. The observed heterogeneity of geological features in the study catchment helped in the interpretation of the experimental dataset. In particular, the possible influence of geology on network presence and persistence was assessed by comparing, for each geologic unit, the contribution to the local drainage density of reaches with different persistency.

To analyze emergent spatial patterns of the flowing stream network, in line with van Meerveld et al. (2019), for each field survey, we also produced spatial maps of the unchanneled length  $L_h$ .  $L_h$  was defined as the distance, along flow directions, from any given point of the catchment to the first point belonging to the active network. The temporal changes of  $L_h$  were analyzed by looking at the catchment average of  $L_h$  and its spatial coefficient of variation as a function of *ADNL*. The frequency distribution of  $L_h$  across the contributing catchment,  $p_L(L_h)$ , was also calculated for each survey. The local variability of  $L_h$  is then assessed by mapping the spatial distribution of the differences between the maximum and minimum value of  $L_h$ , which correspond to the shortest and longest surveyed networks, respectively. These changes in  $L_h$  were first calculated in terms of length (i.e., in meters) and then made dimensionless through the maximum value of  $L_h$  computed in each pixel during the study period.

#### 2.5. Modeling the Active Drainage Network Length

Three different empirical models for the description of *ADNL* were developed, and their performance was formally compared to elucidate the major climatic controls on active network dynamics.

Rainfall depth  $h$  (mm) and potential evapotranspiration  $ET_0$  (mm) at daily scale are the two model inputs. The latter was evaluated from climatic data through the Penman-Monteith equation (Allen et al., 1998).

##### 2.5.1. Model 1

The first model uses the cumulative precipitation  $h_T$  (mm) as the unique explanatory variable for *ADNL*.  $h_T$  was calculated as the sum of antecedent precipitation over a time period of  $T$  days:

$$h_T(t) = \int_{t-T}^t h(\tau) d\tau, \quad (1)$$

where  $t$  is the time to which  $h_T$  is referred and  $\tau$  is the integration variable. The *ADNL* was then modeled with the formula:

$$ADNL(t) = k_0 + k_1 \cdot h_T(t), \quad (2)$$

where the parameters  $k_0$  (km) and  $k_1$  (km/mm) are the intercept and slope of the recession line, respectively, which represent the length of the permanent drainage network and the *ADNL* increase per unit of  $h_T$ .

Three model parameters ( $T, k_0, k_1$ ) need to be calibrated in this model. For any given period  $T$ , a linear regression of the observed *ADNL* against the corresponding  $h_T$  was used to calibrate the parameters  $k_0$  and  $k_1$  of Equation (2), and the goodness of fit was assessed through the coefficient of determination  $R^2$ , calculated

based on all the available observations. Subsequently, the optimal value of  $T$  was selected by maximizing the function  $R^2(T)$ . The robustness of the parameter estimation was checked via leave-one-out cross-validation. This technique consists in repeating the calibration procedure for different training subsets of the available data, each of which is obtained by removing a single data point from the complete data set. The final calibrated parameters are then the average of the parameters obtained from each training subset. To characterize model performance, the standard deviations of the calibrated parameters and the mean absolute model error were calculated.

### 2.5.2. Model 2

The second model was obtained by replacing in equation (1) the cumulative rainfall depth,  $h_T$ , with the cumulative of excess rainfall,  $EP_T$  (mm), that is, the cumulative difference between daily precipitation and evapotranspiration over a period of  $T$  days.

The reference crop evapotranspiration  $ET_0$  was estimated with the Penman-Monteith equation (Allen et al., 1996; Settin et al., 2007). Then a dimensionless crop coefficient  $k_c$  was used to estimate the actual evapotranspiration  $ET$  as

$$ET = k_c \cdot ET_0. \quad (3)$$

In general,  $k_c$  depends on crop type and development stage, and therefore, it should be variable both in space (as a function of land cover) and in time (as a function of the vegetative state). The two main land covers of the Valfredda catchment are grazing pastures and conifer trees, for which the suggested values for  $k_c$  are between 0.85 and 1 throughout the study period (Allen et al., 1998). Therefore, in this work, a uniform and constant  $k_c$  was calibrated in order to link spatially and temporally averaged vegetation conditions to the event-based dynamics of the overall stream length. Also, in this region, soil water content is typically higher than the incipient stress point. Accordingly, equation (3) does not include the effect of water stress on  $ET$ . Nevertheless, the calibrated value of  $k_c$  should implicitly include the possible effect of reduced soil-water availability on catchment-scale evapotranspiration.

The daily excess precipitation was thus expressed as  $EP(t) = h(t) - ET(t)$ . The cumulative excess precipitation,  $EP_T$  (mm), was then calculated by integrating  $EP$  over the period  $T$  as

$$EP_T(t) = \int_{t-T}^t EP(\tau) d\tau. \quad (4)$$

Note that  $EP$  and  $EP_T$  can take negative values when evapotranspiration is bigger than precipitation.

The basic equation of this model is analogous to equation (2):

$$ADNL = k_0 + k_1 \cdot EP_T. \quad (5)$$

This model involves four parameters: the crop coefficient  $k_c$  (equation (3)), the reference aggregation time  $T$  (equation (4)), the length of the permanent drainage network  $k_0$ , and the  $ADNL$  increase per unit of  $EP_T$ ,  $k_1$  (equation (5)).

The calibration was performed following the same procedure used for Model 1: For any given combination ( $T, k_c$ ), the parameters  $k_0$  and  $k_1$  were estimated via linear regression of the observed  $ADNL$ s against the corresponding values of  $EP_T$ ; The goodness of fit was evaluated through the determination coefficient  $R^2$ . The estimation of the optimal values of  $T$  and  $k_c$  was then performed maximizing the function  $R^2(T, k_c)$ . The calibration over the full set of available data was then cross-validated with a leave-one-out technique.

Including  $ET$  in the calculation of the predictor for  $ADNL$  should improve the representation of the shrinking of the active drainage network during recessions. This model, in fact, is expected to originate a decrease of  $ADNL$  over time right after each rainfall event because of the negative values of  $EP$  during non-raining days. During wet periods, instead,  $ET$  is typically smaller than the rainfall amounts, also because of lower temperatures and reduced solar radiation associated to rainy days, thereby leading to an arguably smaller impact of  $ET$  on network dynamics. Note that for  $k_c = 0$ , Model 2 corresponds to Model 1.

### 2.5.3. Model 3

The third model was used to assess the possible influence of different flow generation processes (surface and subsurface flow/groundwater) on the length of the drainage network. Accordingly, two cumulative rainfall

depths (with two different time periods  $T_1$  and  $T_2$ ) were used to predict the active drainage network length as

$$ADNL = k_0 + k_1 \cdot h_{T_1} + k_2 \cdot h_{T_2}. \quad (6)$$

The rationale of this model is the existence of multiple nested expansion/contraction cycles of the active drainage network driven by the cumulative rainfall at different time scales. These time scales possibly correspond to the time scales of the different stream flow generation processes active in the study basin.

The parameters of this model can be divided in two groups: the aggregation time scales  $T_1$  and  $T_2$  used to calculate the cumulative precipitations and the three coefficients ( $k_0$ ,  $k_1$ , and  $k_2$ ) of equation (6).

The calibration procedure was analogous to the previous cases: For any given combination ( $T_1$ ,  $T_2$ ), the parameters of equation (6) were estimated via linear regression, and the corresponding  $R^2$  was evaluated; the optimal value of the couple ( $T_1$ ,  $T_2$ ) was then selected by maximizing the function  $R^2(T_1, T_2)$ , and the calibration was cross-validated with a leave-one-out technique.

The two predictors  $h_{T_1}$  and  $h_{T_2}$  used in equation (6) are different aggregations of the same data, and thus, they could display collinearity effects. When collinearity exists, the estimate of the regression coefficients would become very sensitive to small changes in the available data, thereby reducing the statistical significance of the model. For this reason, the Belsley test (Belsley, 1991) was carried out on the predictor variables to check the possible presence of collinearity between  $h_{T_1}$  and  $h_{T_2}$  for the calibrated values of  $T_1$  and  $T_2$ .

#### 2.5.4. Model Selection

Model selection was carried out based on Akaike weights. This method combines model performance (by minimizing the log of the residual square sum, RSS, between model estimates and experimental data) and model complexity (accounting for the number of calibrated parameters of the model). First, the Akaike information criterion, corrected for small sample sizes, was calculated as (Akaike, 1974)

$$AIC_c = 2 \cdot \frac{g+1}{n} + \log\left(\frac{RSS}{n}\right) + 2 \cdot g \cdot \frac{g+1}{n-g-1}, \quad (7)$$

where  $n$  is the sample size and  $g$  is the number of calibrated parameters.

Akaike weights,  $AW_m$ , were then calculated for each model  $m$  as

$$AW_m = \frac{\exp(-\Delta AIC_{c,m}/2)}{\sum_m \exp(-\Delta AIC_{c,m}/2)}, \quad (8)$$

where  $\Delta AIC_{c,m}$  is the difference between  $AIC_c$  for model  $m$  and the minimum value of  $AIC_c$  among all the models. The optimal model is the one characterized by the lowest value of  $AIC_c$  that coincides to the highest value of  $AW$ . Akaike weights are used for a formal assessment of the best model, as they formally represent the relative likelihood of each model.

### 3. Results

#### 3.1. Analysis of Climatic Data

Precipitation data were analyzed to characterize the climatic regime observed in the study area during the 2018 field campaign and to compare it with the longer term regime in the decade 2010–2019.

The total annual precipitation in 2018 was about 1,500 mm, very close to the annual average in the longer term. Figure 2 (upper panel) shows the daily precipitation time series for the whole 2018.

During the survey period (i.e., from July to November), the total precipitation was 880 mm (a value that is slightly larger than the corresponding longer term average) reflecting a relatively wet fall season, with almost 300 mm of precipitation fallen during the last week of October. Nonetheless, the study period covers a wide range of hydrological states of the catchment, encompassing wet conditions (such as those observed in July or during the first week of November) and relatively dry conditions (such as those recorded in the early fall, when rainfall is less frequent).

The lower box plots in Figure 2 report the average daily precipitation height  $\alpha$  (mm) and the average rainfall frequency  $\lambda$  ( $d^{-1}$ ) for all the months of the year during the longer term period. As typical of the alpine climate, precipitation intensity is quite constant throughout the year, with the exception of late autumn



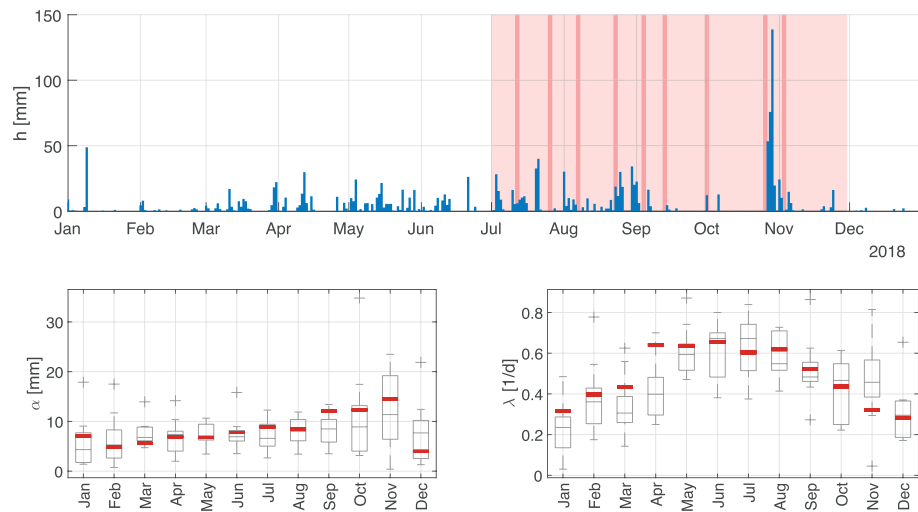


**Figure 2.** Time series of daily precipitation for 2018 (top). The red shaded area highlights the study period, with each field survey indicated by a red vertical line. Box plots of average daily precipitation depth  $\alpha$  and frequency  $\lambda$  by month (bottom) for the years 2010 to 2019. The red horizontal lines represent the averages for 2018, calculated on a 3-month window centered on each month.

when isolated heavy rainfall events might take place. Rainfall frequency  $\lambda$  follows an annual cycle with a minimum in winter and very frequent precipitation events during the summer. The specific values of  $\alpha$  and  $\lambda$  observed during 2018, when the surveys were performed, are also reported in Figure 2 as red horizontal lines and appear to be generally consistent with the corresponding longer term averages during the entire reference decade (2010–2019).

Daily rainfall depth  $h$  and precipitation interarrival times (i.e., the time interval between two subsequent rainy days) were also studied by means of frequency analysis (Figure 3). The annual data were subdivided into two disjoint datasets: the summer-fall period, corresponding to the months when the surveys were performed (July to November), and the rest of the year (from December to June). Available data were analyzed for the longer term period (2010–2019) and for the year 2018 only. The plots shown in Figure 3 indicate that the frequency distributions of  $h$  and interarrivals during the survey period (July–November 2018) are similar to those obtained in the longer term (July–November of all years between 2010 and 2019). Likewise, these frequency distributions are not much different from the distributions obtained for the entire period of record in the months from December to June. The major difference is an increase of the interarrivals during winter and spring, as a byproduct of the winter regime in which precipitation events are less frequent. Conversely, in the months from July to November, the distribution of the rainfall depths has a heavier tail due to the strong precipitation events that take place in late autumn.

The rain amount observed in 2018 is in line with the longer term average, though with a less standard temporal distribution across the months (as implied by the wetter fall). Our analysis also indicates that from July to November 2018, the catchment experienced a variety of hydrological conditions that properly reflect the intra-annual variability of climate conditions typical of this region.

### 3.2. Network Delineation

The *ADNL* observed during different field surveys ranges from 5.5 to 12.2 km (33% to 77% of the maximum potential length as defined in Section 2.2), depending on the underlying hydrological conditions, with an average of 9.1 km (Table 1). The corresponding active drainage density ranges between 1.06 and 2.35 km<sup>-1</sup>. The connectivity of the observed drainage network is reported in Table 1 in terms of disconnected *ADNL* and disconnected clusters (i.e., number of contiguous parts of the active network that are disconnected from the outlet). The minimum *ADNL* (Figure 4a) was surveyed on the 26th of October, after a dry period of about 50 days (total precipitation 38 mm). The maximum extension of the active drainage network was recorded 8 days later, on the third of November, after a precipitation event of about 320 mm (Figure 4b).

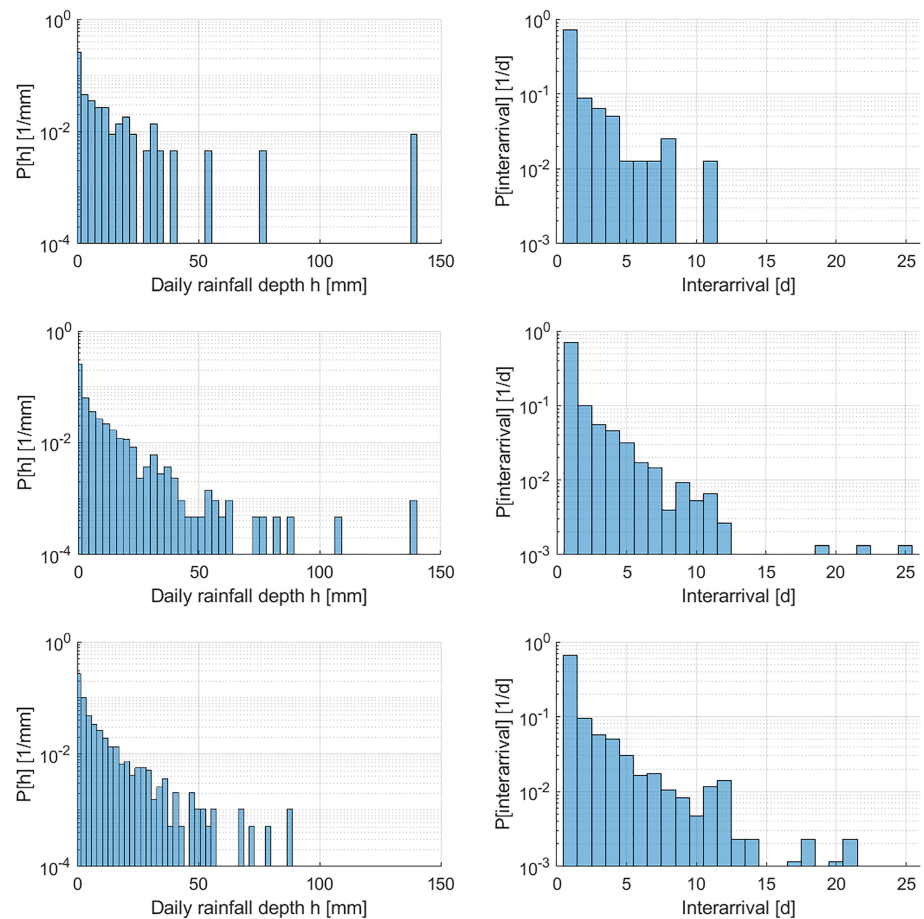
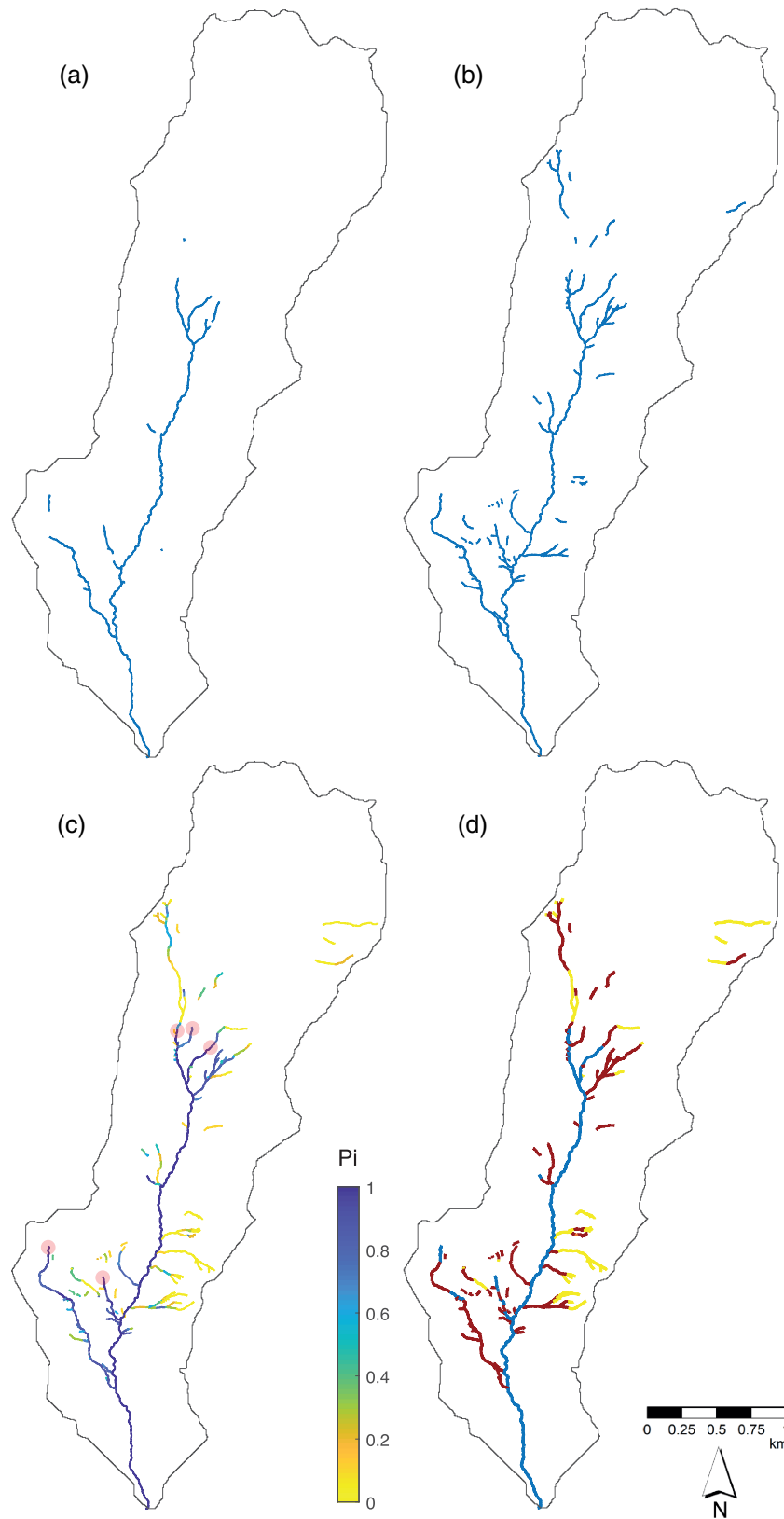


**Figure 3.** Frequency analysis of daily rainfall depth  $h$  (left) and precipitation interarrival (right). The top plots refer to the study period (July to November 2018), the middle plots refer to the corresponding long term period (July to November from 2010 to 2019), and the bottom plots refer to the rest of the year (December to June, 2010–2019).

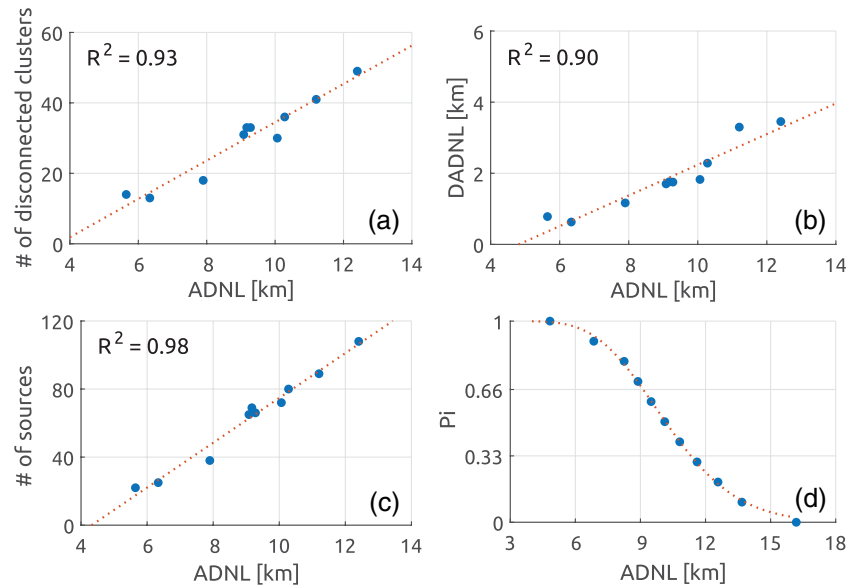
The spatial distribution of the persistency index,  $P_i$ , is represented in Figure 4c. The lower order branches of the network generally have a lower persistency, with the exception of the tributaries that are supplied by permanent springs, marked on the figure with pale red circles.

The permanent fraction of the drainage network covers only 28% of the total length (Figure 4d), suggesting a high temporal variability of the drainage network notwithstanding the humid climate and the presence of many permanent springs in the catchment. Despite showing evident channelization signs, 21% of the potential length was inactive during all the field surveys.

Figure 5 shows how the number of disconnected clusters, the number of sources, the disconnected  $ADNL$ , and the persistency index  $P$  vary as a function of  $ADNL$ . As  $ADNL$  increases, two contrasting processes can affect the number of disconnected branches of the network. On one hand, in the presence of active streams that are only temporarily disconnected from the outlet due to a dry channel downstream, an increase in  $ADNL$  should remove the disconnections, thus reducing both the number of disconnected clusters and the disconnected  $ADNL$ . On the other hand, in case of temporary stretches that remain always disconnected from the main river network, an increase in  $ADNL$  during wetting produces the activation of new disconnected reaches, thereby increasing both the number of disconnected clusters and the disconnected  $ADNL$ . The increasing trend of disconnected clusters and disconnected  $ADNL$  as function of  $ADNL$  shown in Figure 5 therefore indicates that in the Valfredda catchment the activation of additional disconnected reaches during river network expansion dominates. Accordingly, also the number of sources increases with  $ADNL$  because the less persistent stretches (which become active only for high values of  $ADNL$ ) mostly correspond to the lower order upstream channels, where the network is more branched (see Figure 4c).



**Figure 4.** Maps of the Valfredda drainage network: (a) active drainage network at its minimum on 26/10/2018, (b) active drainage network at its maximum on 03/11/2018, (c) persistence index, from 0 (yellow) to 1 (blue) and (d) classification of network stretches as persistent (blue), temporary (red) and dry (orange). Red circles in panel (c) denote permanent springs. Panels (c) and (d) show the potential network; disconnections are present when channels stop and the water flow is dispersed on the hillslope and infiltrated.



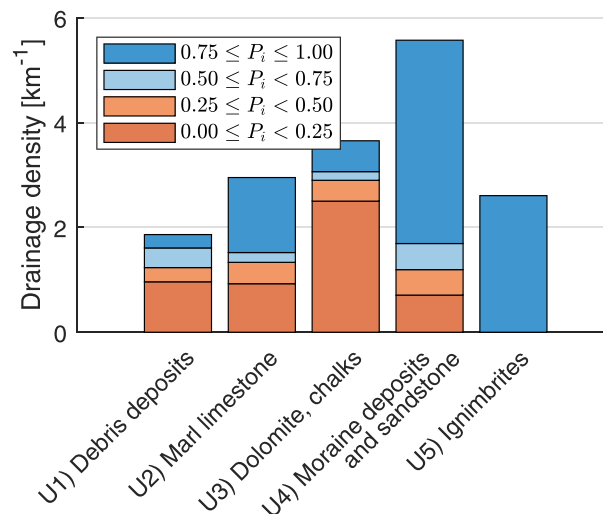
**Figure 5.** Correlation between key properties of the drainage network. Number of disconnected clusters (a), disconnected active drainage length (b), and number of sources (c) are linearly correlated with ADNL. Persistence  $P_i$  follows a gamma distribution with  $k = 15.8$  and  $\theta = 0.67$  km (d). The red dotted lines represent the regression line (panels a, b, c) and the theoretical gamma distribution (panel d). The  $P$  value of each regression is smaller than  $10^{-3}$ .

Figure 5d shows the relationship between  $ADNL$  and the persistency index  $P_i$ . The plot shows the length of the active drainage network obtained when only the stretches with persistency greater than (or equal to) different values of  $P_i$  are active. The observed points closely follow a gamma distribution with shape parameter  $k = 15.8$  and scale parameter  $\theta = 0.67$  km.

### 3.3. Spatial Patterns of Drainage Density and Unchanneled Lengths

Based on the geological features of the bedrock, five different geologic units were detected in the study catchment: (U1) solid and debris limestones, moraine and debris deposits; (U2) marl limestones; (U3) dolomite and chalks; (U4) moraine deposits and sandstone; and (U5) rhyodacitic ignimbrites. The heterogeneity in the geology is also reflected in the soil cover and vegetation (see below).

A significant spatial variability in the drainage density and network dynamics was observed across the five geologic units (Figure 6). In the northern part of the catchment (U1), where debris deposits and terrain



**Figure 6.** Drainage density in the five main geologic units of the catchment, classed based on the underlying persistency.



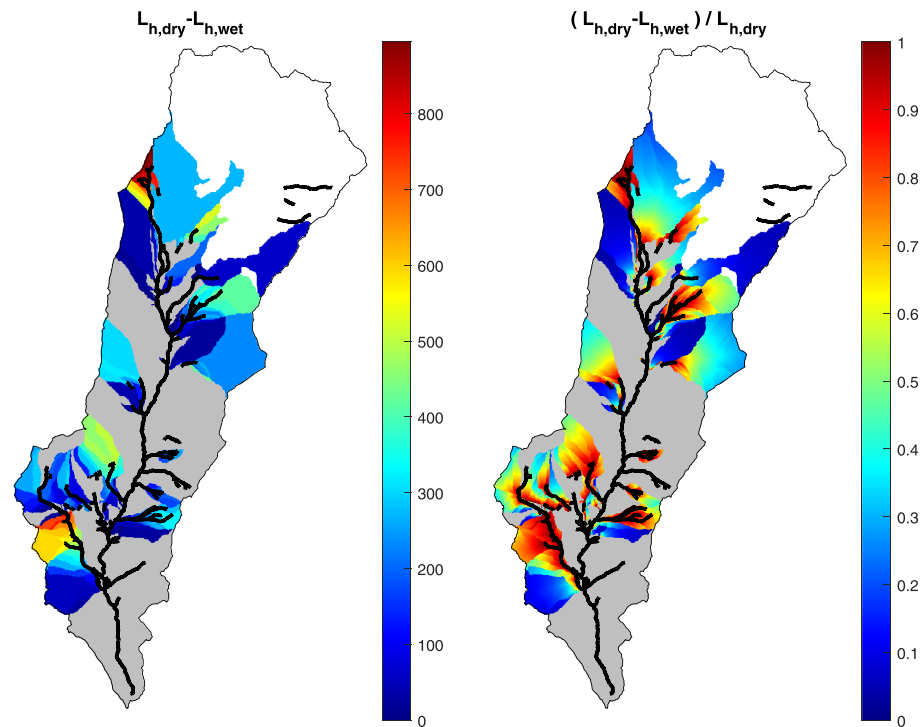


**Figure 7.** Maps of the variation of  $L_h$  between the wettest and driest network, in meters (left) and as a fraction relative to the driest network (right).

depressions dominate, the drainage density is low (namely,  $1.9 \text{ km}^{-1}$ , of which  $1.3 \text{ km}^{-1}$  has a persistency smaller than 0.5). This is also reflected by the presence of several pits in the DTM, some of them characterized by relatively high contributing areas, where water can accumulate during rainfall events to be later infiltrated and transferred to the groundwater.

In the portion of the catchment between 1,800 and 2,150 m a.s.l. (U2), we observed five perennial sources fed by groundwater (pale-red dots in Figure 4), possibly originating from the northern part of the basin. These permanent streams represent the nondynamical fraction of the network. However, they can be enriched by a multitude of temporary tributaries during wet conditions (Figures 4a–4c). In this geologic unit, the drainage density ( $3 \text{ km}^{-1}$ ) is almost evenly contributed by persistent and temporary streams (Figure 6). These dynamic tributaries can either expand upstream from the most permanent reaches of the network or expand downstream from disconnected reaches that temporarily reconnect to the main Valfredda creek during wet conditions.

The most dynamical reaches of the network were observed in the central-eastern region of the watershed (U3), where rocky outcrops dominate. Interestingly, the tributaries that are located on the western side of the catchment (U4) were much less dynamical. This asymmetry in the temporariness of the tributaries that originates from the two hillslopes of the main valley in the central part of the catchment is explained by the heterogeneity of geology and physiography. The western side of the valley is characterized by moraine deposits overlaid by a relatively thick organic soil layer covered by grassland and conifers (Figure 1). This part of the catchment shows a high drainage density ( $\approx 5.5 \text{ km}^{-1}$ ), of which only  $1.2 \text{ km}^{-1}$  has a persistence smaller than 0.5 (Figure 6). Instead, on the eastern side, the dolomite bedrock is close to the surface and generates an almost-impermeable surface with steep slopes. The resulting network has a much lower persistency, and drainage density is much smaller than in U3 ( $3.6 \text{ km}^{-1}$ ). Finally, the lower part of the main valley (U5) is covered by thick forest. Here, the drainage density is reduced to  $2.6 \text{ km}^{-1}$ , and all channels are persistent.

The observed spatial variability of the drainage density is also reflected in the spatial distribution of the unchanneled lengths across the whole contributing catchment and in its temporal dynamics. The detailed maps of unchanneled lengths associated to different network configurations are shown in the supporting

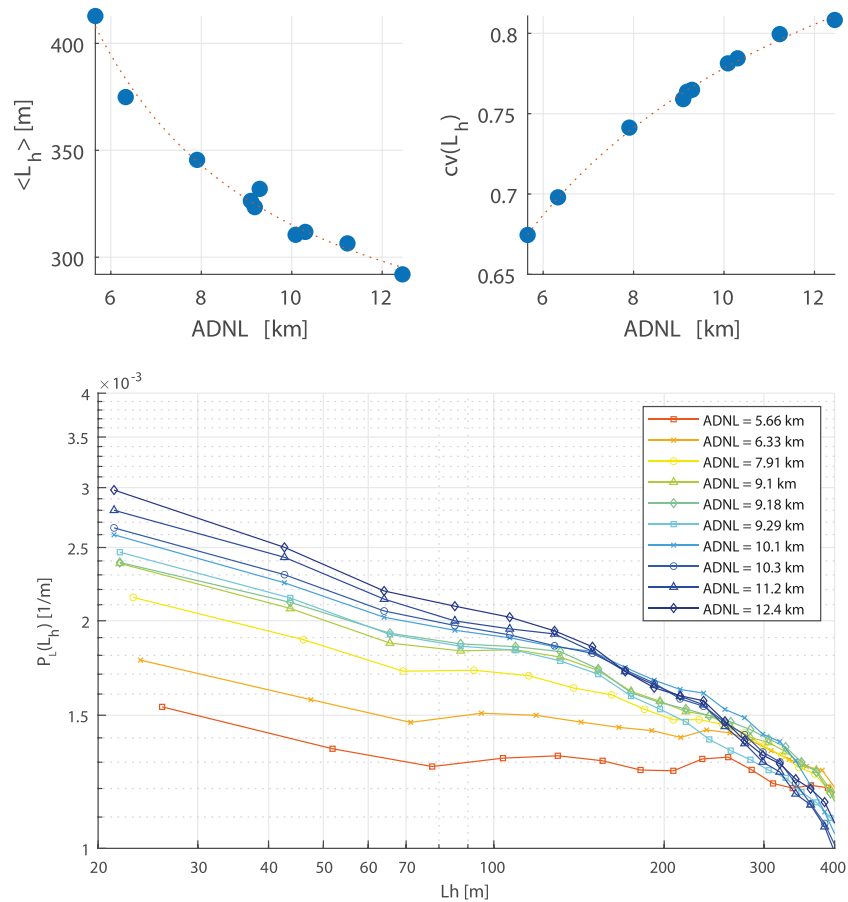


**Figure 8.** Average and coefficient of variation of  $L_h$  as a function of  $ADNL$  (top). Frequency distributions of  $L_h$  (bottom).

information. Figure 7, instead, shows the spatial distribution of the total (i.e., in terms of length) and relative (i.e., in terms of percentage) differences of  $L_h$  calculated comparing the wettest and the driest configurations of the stream network during the study period. The total length differences are nearly uniform throughout the different subcatchments drained by each temporary stream (Figure 7a). This happens because when a temporary stretch is activated, all the pixels belonging to the pertinent upstream contributing area experience a similar reduction of  $L_h$  (that roughly corresponds to the length of the activated stretch). Instead, the relative differences (here calculated with respect to the driest network) are bigger for the pixels closer to the network and smaller for the pixels near the divides. Noticeably, a large portion of the catchment experiences no changes in the unchanneled length (grey areas in Figure 7). These are the pixels drained by the permanent reaches of the stream network that are mainly located along the main valley in the middle part of the watershed and in the southern portion of the catchment.

Figure 8 shows the mean and the spatial coefficient of variation (CV) of  $L_h$  as a function of  $ADNL$ . As expected, the average  $L_h$  decreases when  $ADNL$  increase (i.e., for wetter networks the mean hillslope length is smaller). The decreasing trend of the mean  $L_h$  is nonlinear, with higher changes for smaller values of  $ADNL$ . In fact, changes in network length affect larger portions of the drainage area when the network is shorter. The coefficient of variation of  $L_h$ , instead, weakly increases with  $ADNL$  because the network expansion takes place in a nonuniform manner, with many temporary streams that are clustered in relatively small portions of the catchment. This result indicates that the stream network becomes more heterogeneous during its expansion.

The frequency distributions of  $L_h$ ,  $p_L(L_h)$ , corresponding to each surveyed network, are reported in Figure 8. All the distributions show higher frequencies for small values of  $L_h$ . However, smaller  $ADNL$  values are associated with lower probabilities of small  $L_h$ . The decreasing trend of  $p_L$  with  $L_h$ , shared by all the curves,

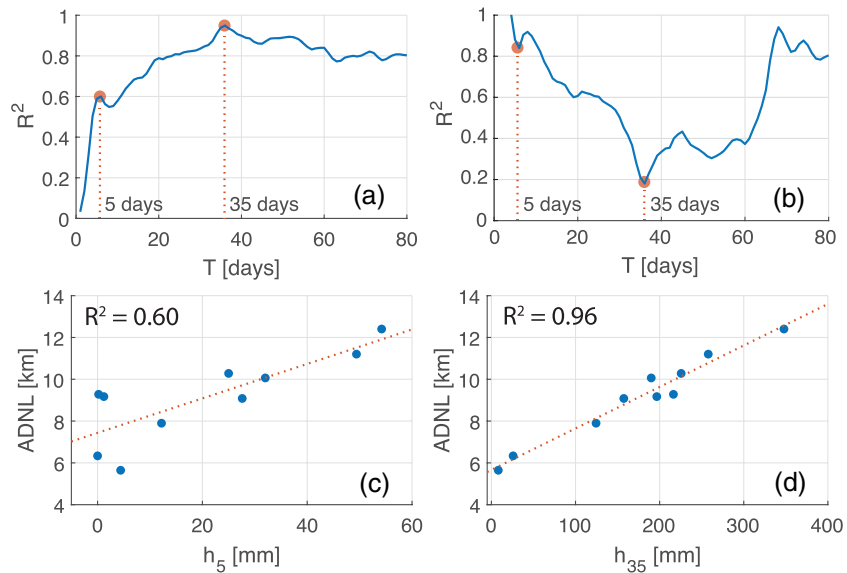


**Figure 9.** Performance of Model 1 as a function of time period  $T$  in terms of  $R^2$  (a) and MAE (b). Scatter plots of ADNL versus  $h_T$  for the two time periods of 5 and 35 days (panels c and d, respectively); the blue points correspond to field surveys, the orange dotted line is the linear regression. The  $P$  value of the linear regression is smaller than 0.015 for  $4 \leq T \leq 66$  days, and smaller than 0.05 in all other cases.

is more pronounced for longer networks. Instead, for the driest network, the pdf of  $L_h$  tends to become uniform, in line with previous results (van Meerveld et al., 2019).

### 3.4. Modeling ADNL

The performance of the different models described in Section 2.5 was assessed through the  $R^2$  and the MAE of the linear regression between the observed and predicted ADNL during the surveys carried out from July to November 2018. Despite its simplicity, Model 1 provides a good description of ADNL, with a  $R^2$  of 0.96 (Figure 9). The values of the calibrated parameters are reported in Table 2, together with the mean and variance of ADNL during the study period, the Akaike index and the corresponding Akaike weight. Figure 9a shows  $R^2$  and MAE as function of the aggregation time scale for rainfall ( $T$ ) in Model 1. Two different local maxima of  $R^2$  can be recognized: a first, narrow peak for  $T = 5$  days ( $R^2 \simeq 0.67$ ) and a second peak, much higher and wider, for  $T = 35$  days ( $R^2 = 0.96$ ). The same pattern is found in the MAE, for which two local minima can be identified for the same aggregation time scales mentioned above. This suggests the simultaneous presence of multiple expansion/contraction cycles of the active drainage network operating at different time scales (i.e., 5 and 35 days).

Figure 9c shows the scatter plot of ADNL against  $h_5$ , which is the cumulative rainfall observed during the 5 days prior to each survey. Data points appear to be aligned quite well along the regression line for high values of  $h_5$ , while they are more scattered for small values, probably because after 5 days of little or no precipitation, the hydrological condition of the catchment is dictated by slower hydrological processes that are more affected by long-term precipitation patterns. On the other hand, when a considerable rainfall event occurs, a significant fraction of the network is impacted by faster hydrological dynamics, which are in turn affected by short-term precipitation.

The scatter plot of ADNL against  $h_{35}$ , the cumulative precipitation in the 35 days before each survey, is reported in Figure 9d. In this case, all the points are well aligned on the regression line, and the model performance increased ( $R^2 = 0.96$ ) relative to the case in which  $h_5$  was used as a predictor for ADNL. The increased performance of the model suggests that, at the catchment scale, the river network dynamics are mainly controlled by processes occurring on monthly time scales. Further, note that  $h_{35}$  can be seen as the sum of  $h_5$  and the precipitation from 5 to 35 days prior to the surveys. Thus,  $h_{35}$  includes, to some extent, the cumulative effect of the variability of short-term and long-term precipitation. As a result, the Pearson correlation coefficient between  $h_5$  and  $h_{35}$  is 0.73.

**Table 2**  
Comparison of the calibrated parameters and performances (in terms of  $R^2$  and Akaike weights) of the different models

Model	# of calibrated parameters	Regression parameters	$R^2$	MAE	ADNL	$AIC_c$	AW		
1a	3	$T$	5	days	0.64	$1.17 \pm 0.81$	$8.9 \pm 4.4$ km	5.1	0.224
		$k_0$	$7.4 \pm 0.3$	km					
		$k_1$	$0.082 \pm 0.008$	km/mm					
1b	3	$T$	35	days	0.96	$0.40 \pm 0.20$	$8.1 \pm 2.4$ km	2.9	0.688
		$k_0$	$5.7 \pm 0.07$	km					
		$k_1$	$0.020 \pm 0.0004$	km/mm					
2	4	$T$	35	days	0.96	$0.40 \pm 0.20$	$8.1 \pm 2.4$ km	7.1	0.084
		$k_c$	0	-					
		$k_0$	$5.7 \pm 0.07$	km					
		$k_h$	$0.020 \pm 0.0004$	km/mm					
		$T_1$	5	days					
		$T_2$	35	days					
3	5	$k_0$	$5.8 \pm 0.09$	km	0.99	$0.28 \pm 0.20$	$8.2 \pm 2.6$ km	13.3	0.004
		$k_1$	$0.022 \pm 0.0002$	km/mm					
		$k_2$	$0.017 \pm 0.0005$	km/mm					

Note. Model 1 is presented twice, considering for the parameter  $T$  both the local optimum of 5 days and the global optimum of 35 days.

Compared to Model 1, Model 2 introduces the effect of evapotranspiration through the parameter  $k_c$ . Figure 10 shows  $R^2$  and MAE as function of the two calibration parameters,  $T$  and  $k_c$ , for Model 2. Model performance generally decreases for larger values of  $k_c$  and reaches its maximum for  $k_c = 0$ , a value for which this model corresponds to Model 1. For fixed values of  $k_c$  (i.e., along horizontal lines in the plot of Figure 10), the patterns of  $R^2$  (and MAE) are the same as in Model 1, with a wide peak around  $T = 35$  days and high values of  $R^2$  up to  $T = 60$  days.

The performance of Model 3 as a function of the time periods  $T_1$  and  $T_2$  is shown in Figure 11, where  $R^2(T_1)$  exhibits a peak for  $T_1 = 5$  days and a global maximum at  $T_1 = 35$  days and  $R^2(T_2)$  follows the same pattern, generating the maximum  $R^2$  for  $T_2 = 35$  days. As a consequence, the optimal combination of  $T_1, T_2$  is (5, 35) days. This model reaches  $R^2 = 0.99$ , further improving the performance of Model 1 because it simultaneously accounts for processes happening on two different time scales. The Belsley collinearity test between the cumulative precipitation for the two relevant time periods identified by calibration produces a maximum scaled condition index around 3, indicating that collinearity is not an issue for the given model.

All the models were validated through a leave-one-out cross validation technique. As reported in Table 2, the standard deviation of the calibrated parameters is very small, originating coefficient of variations (CV) for each model parameter in the order of 0.01. The small variability of the parameters on different training

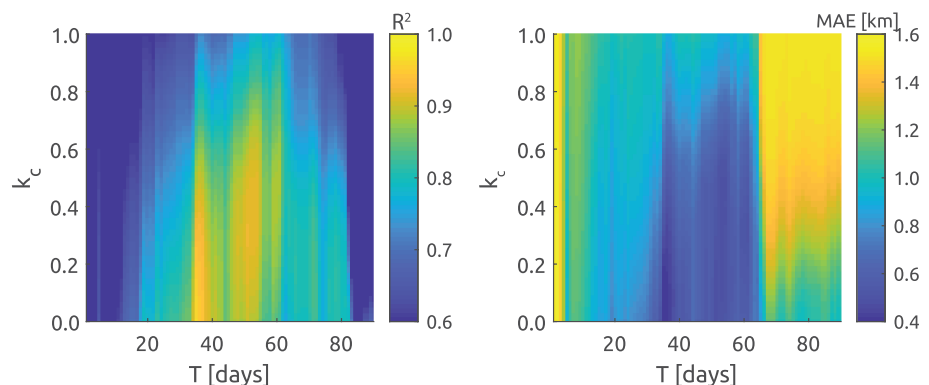


**Figure 10.**  $R^2$  and MAE of Model 2 as a function of time period  $T$  and crop coefficient  $k_c$ .



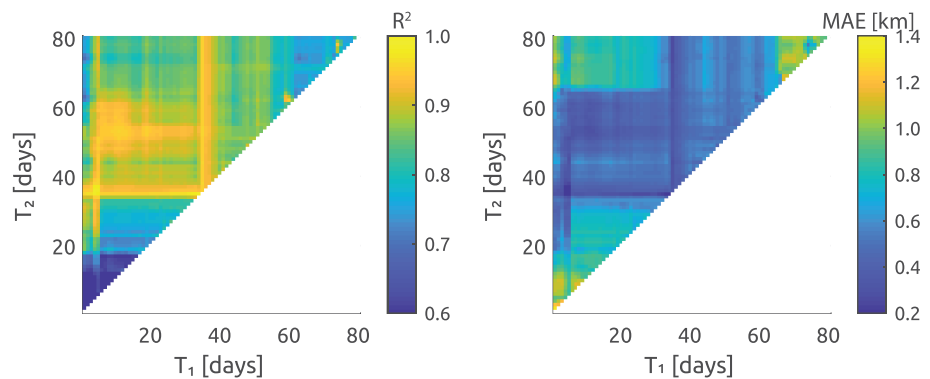


**Figure 11.**  $R^2$  and MAE of Model 3 as a function of the two time periods  $T_1$  and  $T_2$ .

subsets is an indicator of the robustness of the models. Table 2 also shows the MAE and its standard deviation for each calibrated model. The MAE coefficient of variation is very small, indicating the robustness of the approach regardless of the specific calibration subset chosen for calibration. The mean MAE exhibits the same pattern of  $R^2$ , being smaller for Model 3 and higher for Model 1, particularly when using  $h_5$  as predictor variable.

The additional survey performed on 18 January 2019 was used to get a preliminary indication of the performance of each model during winter conditions, when snow dynamics affect the hydrology of the site. Model 1 shows the smallest absolute error, 0.19 km, when  $h_{35}$  is used as independent variable, while the same model produces the highest error (1.9 km) with  $h_5$  used as a predictor of *ADNL*. This is arguably related to the effect of snow storage that impacts the water balance during relatively short time scales. Model 3, which combines the two predictors together, has an absolute error of 0.3 km. These errors are comparable to the MAE of the models during the calibration/validation period, suggesting that the same approaches might be valid also during the winter season. However, more data are needed to confirm this hypothesis.

### 3.5. Model Ranking

The different models were formally ranked using the Akaike weights (*AW*), as reported in Table 2. Table 2 also shows the permanent *ADNL* (as described by the regression parameter  $k_0$ ) and the mean and variance of *ADNL*. Model 1b is the best model, according to the Akaike weights, as it is able to provide a good description of the dynamics of *ADNL* using a limited number of parameters. Model 2 has one parameter more than Model 1, with no performance improvement. In fact, the Model 2 calibration results in  $k_c = 0$ , for which the behavior is the same as Model 1. As a result, Model 2 has a lower *AW* than Model 1 because the same performance can be obtained with less parameters. Model 3 allows a slight increase in model performance, though it requires two additional parameters. As a consequence, Model 1 has a significantly better rating than the other models, since it represents the optimal trade-off between goodness of fit and model complexity.

The simulated *ADNL* time series for Models 1 and 3 are compared in Figure 12. The main differences occur during and shortly after the major precipitation events; this is particularly visible for the large rainstorm at the end of October. Such differences are due to Model 3 being able to better capture the expansion/contraction cycles of the active drainage network in response to short-term and long-term precipitation. Model 1, on the other hand, only captures long-term *ADNL* variability induced by monthly rainfall dynamics, and it is likely to underestimate the actual short-term temporal variability of *ADNL*.

## 4. Discussion and Conclusions

This study presents the results of an intensive campaign for the field mapping of the stream network conducted over a relatively large catchment ( $>5 \text{ km}^2$ ) with a high temporal resolution (for a total of about  $12.5 \text{ km}^2/\text{month}$  of catchment surveyed, with an average of one survey every 14 days). Our data confirm previous results obtained in other climatic and geographic settings about the highly dynamical nature of river networks (e.g., Buttle et al., 2012; Datry et al., 2014; Godsey & Kirchner, 2014; Jensen et al., 2017). In particular, notwithstanding the humid climate typical of the Alps, more than 72% of the stream network in the Valfredda catchment is dynamic, with an observed drainage density that varied, during about 6 months,

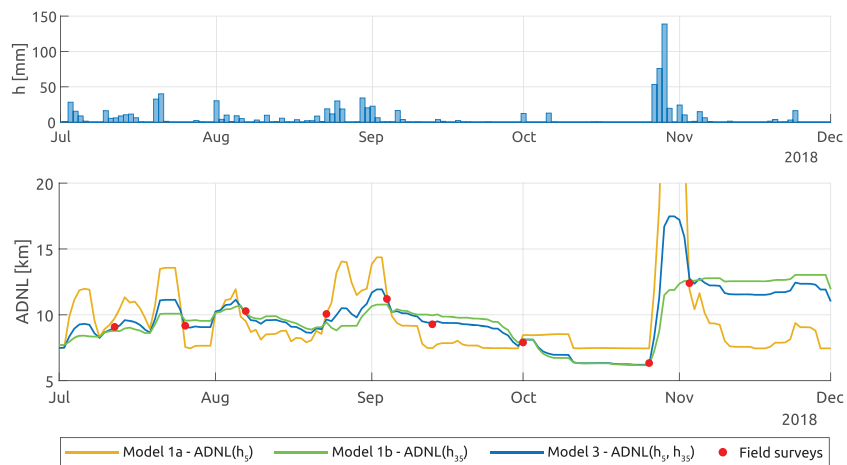


**Figure 12.** Comparison of the calibrated models. The top plot shows precipitation during the period from 1 July to 30 November 2018. The bottom plot shows ADNL as calculated by the calibrated models. Model 2 is not reported as it is the same as Model 1b. For clarity, ADNL axis has been limited to 20 km even if the maximum length reached by Model 1 is about 32 km.

between 1 and  $2.5 \text{ km}^{-1}$  depending on the underlying hydrological conditions. Under wet conditions, a considerable increase in the disconnected clusters and sources was also observed. This circumstance hints at the importance of mapping not only the streams directly connected to the outlet but also all the channels that may be temporarily or permanently disconnected. The portion of the network that was mapped as systematically inactive is 21%, suggesting that for many streams, the time scale of wetting/drying cycles may be smaller than 48 hr (the typical lag between a precipitation event and the subsequent field survey in our campaign). Moreover, the expansion/contraction cycles of the active drainage network are strongly controlled by event-scale hydrological dynamics, as indicated by the fact that the transition from the shortest to the longest recorded networks was observed in response to a single, albeit extreme, precipitation event.

The analysis of climatic data indicates that precipitation dynamics in the study period reasonably represent the rainfall regime experienced by the Valfredda stream in the long run. Moreover, during the survey period (July to November 2018), the catchment experienced a variety of hydrological conditions that properly reflect the intra-annual variability of climate conditions typical of this region.

One of the main goals of our study was to quantitatively analyze how the unsteady nature of the climatic forcing controls stream network dynamics. Empirical data and model results indicate that the temporal dynamics of the stream network length are mainly driven by the observed patterns of short- and long-term antecedent precipitation (timing and amount). The comparison of the different models also suggests that evapotranspiration does not affect significantly the observed intra-seasonal changes of stream length in the Valfredda catchment, possibly due to the high runoff ratios typical of this Alpine region and the low percentage of forested areas (almost 30% of the total area).

The advantages of establishing a direct relationship between network length and precipitation (in place of the analogous relationship between network length and discharge already available in the literature) can be manifold. Streamflow is a spatially and temporally integrated output that in turn depends on precipitation dynamics (Botter et al., 2013; Kirchner, 2009; Nicotina et al., 2008; Rodriguez-Iturbe et al., 1982). Consequently, the discharge observed at the outlet of a given catchment reflects how antecedent precipitation inputs in the contributing area were stored and routed across different landscape units. Here, we have shown that, similarly to streamflow, the river network length at a given time is the byproduct of the antecedent precipitation over a broad range of time scales, from weekly to monthly. Therefore, the existing relationships between discharge and ADNL, although useful to characterize stream length regimes, might be the byproduct of a spurious correlation induced by the presence of common drivers in the two variables (especially rainfall). This possibly hampers the identification of clear causal connections between the local discharge and the upstream active network length. On the other hand, precipitation is a spatially distributed driver perfectly suited to be integrated in time and space and provides useful information about the selective activation of different hydroclimatic processes that underlie network expansion/contraction in river basins.

Our modeling results indicate the presence of multiple expansion and retraction cycles operating at different time scales behind the observed dynamics of the Rio Valfredda stream network. These overlapping dynamics may be in turn controlled by two distinct hydrological processes: (i) quick subsurface flow in the root zone feeding temporary streams and (ii) slower groundwater flow generated by the aquifers supplying water to the less dynamical reaches of the river network. The superposition of dynamics characterized by different time scales could lie at the basis of the hysteresis frequently observed in the relationship between discharge and *ADNL* (Jensen et al., 2018; Prancevic & Kirchner, 2019; Shaw et al., 2017; Ward et al., 2018). In spite of the empirical nature of the link between *ADNL* and precipitation provided in this paper, we believe that our results could provide a preliminary basis to incorporate the simulation of network expansion and contraction in hydrological models using climatic data.

One of the research hypotheses of this paper is that geologic and physiographic features of the catchment dictate the sensitivity of network dynamics to the climatic forcing and the spatial patterns of such dynamics. This study confirms that heterogeneity of geological properties correspond to the observed spatial variability in the active network dynamics of the Valfredda catchment. Depressions, karst areas, and debris deposits with high hydraulic conductivity might decrease the local drainage density, thereby reducing the number and the length of active channels. As karst areas and debris are quite typical features in dolomitic landscapes, we might expect the presence of wide areas with a very low of drainage density to be an ubiquitous feature of Alpine areas in northeastern Italy. Rocky outcrops and shallow soils, instead, promote the generation of a flashy hydrological response dominated by overland flow, which in turn produces temporary streams with a low persistency. Thick, organic soil layers covered by vegetation support the infiltration of rainfall water in the root zone. This water might then be slowly released after each precipitation event, thereby promoting the development of exfiltration processes in the sites where flow paths converge (Beven & Kirkby, 1979), generating stable springs that ensure a high persistency of the downstream channels. Densely vegetated hillslopes hamper erosional processes and surface flow generation and may result in a relatively low drainage density, in which almost all channels are persistent. However, stronger conclusions about network heterogeneity require more comprehensive analyses and more detailed data, such as soil depth and transport capacity, which is not yet available in the study catchment.

The analysis of the distribution of unchanneled lengths under different network configurations revealed a pronounced temporal variability and spatial heterogeneity of the local hillslope length. Significantly, when the river network expands, the spatial heterogeneity of the drainage density is enhanced, which is reflected by higher values of the coefficient of variation of  $L_h$  in our study site. This could be a byproduct of the clustering of the temporary streams of the network that mirrors the spatial heterogeneity of geologic and morphological properties of the landscape. Also, the pdf of  $L_h$  is uniform for shorter networks, while small values of  $L_h$  have higher probability when the network is expanded. This implies that when the network is dry, the hillslope flow paths tend to be convergent, whereas the available unchanneled flow paths are mutually parallel when the stream network is fully developed.

Our analyses suggest that existing hydrological models, based on static (e.g., digitally derived) stream networks, might not be able to capture properly the effects of the local and temporary increase of drainage density produced by precipitation events. Consequently, current models possibly fail in describing the heterogeneous increase in the length of hillslope pathways observed during drying. This dynamical change in the hillslope width function during catchment drying arguably produces an unaccounted source of non-linearity in recession properties, which might be reflected in enhanced recession exponents and/or in an increased interevent variability of recession parameters (Floriancic et al., 2018; Shaw, 2016). We argue that considering the stream network no longer as a predefined input of hydrological models but, rather, as a model output could considerably enhance our capacity to predict and reproduce streamflow regimes, especially in the headwaters. Nevertheless, this will require huge efforts for making experimental data about network dynamics available to the scientific community, thereby allowing the development of novel mechanistic formulations able to describe causes and effects of river network dynamics.

Observed spatiotemporal patterns of stream network dynamics can be efficiently summarized through persistency index maps, which indicate the percentage of time during which every stream of the network is active. These maps provide a useful graphical tool to characterize stream network dynamics and allow fair and objective comparisons across diverse river systems (e.g., Oviden & Gregory, 1980). Broad applications

of these tools can be already foreseen, possibly beyond hydrological sciences. In fact, stream network dynamics are expected to impact a huge number of biogeochemical and ecological processes, including the release of CO<sub>2</sub> from headwater streams to the atmosphere, and the export of carbon and nutrients from uplands to downstream ecosystems (e.g., Battin et al., 2009; Bertuzzo et al., 2017; Dick et al., 2014; Dupas et al., 2019; Ensign & Martin, 2006; Fasching et al., 2016; Helton et al., 2017; Krause et al., 2017; von Schiller et al., 2014). Therefore, the development of coupled hydrological, ecological, and biogeochemical models at the catchment scale that properly account for the stream network variability represents an area where more research is warranted.

Ongoing experimental work in the Valfreda catchment is devoted to extend the field monitoring to longer time periods and design additional campaigns, possibly with the aid of high-tech sensors. Further analyses will also be also performed to study the impact of stream network dynamics on spatiotemporal patterns of water quality and nutrient export.

### Acknowledgments

We thank Andrea Betterle, Anna Carozzani, and Nicola Marigo for their help in performing the field surveys. We are grateful to the Veneto Region and the Veneto Region Environmental Protection Agency (ARPAV) for providing the meteorological data collected by their station, the municipality of Falcade and the Compagnia della montagna di Valfreda - Mònt da le fède for making available the Valfreda catchment for this research project and the Flora Alpina mountain retreat for providing useful help in the field activities. We also thank the anonymous reviewers and the associate editor for all the insightful comments that have been of great help in improving the manuscript.

This study was supported by the European Research Council (ERC) DyNET project funded through the European Community's Horizon 2020 - Excellent Science - Programme (grant agreement H2020-EU.1.1-770999).

The climatic data used in this study can be found on the ARPAV website (<https://www.arpa.veneto.it> Veneto region environmental protection agency (ARPAV)—Climatic data download page, 2019); the Italian geologic map can be found on the ISPRA website (<http://www.isprambiente.gov.it> Superior institute for environmental research and protection (ISPRA)—Italian geologic map sheet 11, 2019); experimental data collected for this study is available at Durighetto et al. (2019).

### References

- Agren, A., Lidberg, W., & Ring, E. (2015). Mapping temporal dynamics in a forest stream network—Implications for riparian forest management. *Forests*, 6(9), 2982–3001. <https://doi.org/10.3390/f6092982>
- Akaike, H. (1974). A new look at the statistical model identification. *Transactions on Automatic Control*, 19, 716–723. <https://doi.org/10.1109/TAC.1974.1100705>
- Allen, R., Pereira, L., Raes, D., & Smith, M. (1998). *Guidelines for computing crop water requirements*. Rome: Food and Agriculture Organization of the United Nations.
- Allen, R., Smith, M., Pruitt, W., & Pereira, L. (1996). Modification of the FAO crop coefficient approach. In *Proceedings of the International Conference* (pp. 124–132). San Antonio, TX.
- Anderson, M., & Burt, T. (1978). Analysis of spatial water quality and stream networks in Southern Cotswolds during and after the drought of 1976. *Earth Surface Processes*, 3, 59–69. <https://doi.org/10.1002/esp.3290030106>
- Battin, T., Luysaert, S., Kaplan, L., Aufdenkampe, A., Richter, A., & Tranvik, L. (2009). The boundless carbon cycle. *Nature Geoscience*, 2, 598–600. <https://doi.org/10.1038/ngeo618>
- Belsley, D. (1991). A guide to using the collinearity diagnostics. *Computer Science in Economics and Management*, 4, 33–50. <https://doi.org/10.1007/BF00426854>
- Berger, E., Haase, P., Kuemmerlen, M., Leps, M., Schaefer, R., & Sundermann, A. (2017). Water quality variables and pollution sources shaping stream macroinvertebrate communities. *Science of the Total Environment*, 587, 1–10. <https://doi.org/10.1016/j.scitotenv.2017.02.031>
- Bernal, S., & Sabater, F. (2008). The role of lithology, catchment size and the alluvial zone on hydrogeochemistry of two intermittent Mediterranean streams. *Hydrological Processes*, 22, 1407–1418. <https://doi.org/10.1002/hyp.6693>
- Bertuzzo, E., Helton, A., Hall, R., & Battin, T. (2017). Scaling of dissolved organic carbon removal in river networks. *Advances in Water Resources*, 110, 136–146. <https://doi.org/10.1016/j.advwatres.2017.10.009>
- Beven, K., & Kirkby, M. (1979). A physically based, variable contributing area model of basin hydrology. *Hydrological Sciences Journal*, 24, 43–69. <https://doi.org/10.1080/02626667909491834>
- Blyth, K., & Rodda, J. (1973). A stream length study. *Water Resources Research*, 9(5), 1464–1461.
- Boodoo, K. S., Trauth, N., Schmidt, C., Schelker, J., & Battin, T. J. (2017). Gravel bars are sites of increased CO<sub>2</sub> outgassing in stream corridors. *Scientific Reports*, 7(1), 1–9. <https://doi.org/10.1038/s41598-017-14439-0>
- Botter, G., Basso, S., Porporato, A., Rodriguez-Iturbe, I., & Rinaldo, A. (2010). Natural streamflow regime alterations: Damming of the Piave river basin (Italy). *Water Resources Research*, 46, W06522. <https://doi.org/10.1029/2009WR008523>
- Botter, G., Basso, S., Rodriguez-Iturbe, I., & Rinaldo, A. (2013). Resilience of river flow regimes. *Proceedings of the National Academy of Sciences*, 110(32), 12,925–12,930.
- Buttle, J. M., Boon, S., Peters, D. L., Spence, C., van Meerveld, H. J., & Whitfield, P. H. (2012). An overview of temporary stream hydrology in Canada. *Canadian Water Resources Journal*, 37(4), 279–310. <https://doi.org/10.4296/cwrj2011-903>
- Butturini, A., Alvarez, M., Bernal, S., Vasquez, E., & Sabater, F. (2008). Diversity and temporal sequences of forms of DOC and NO<sub>3</sub>– discharge responses in an intermittent stream: Predictable or random succession? *Journal of geophysical research*, 113, G03016. <https://doi.org/10.1029/2008JG000721>
- Cardenas, M. (2007). Potential contribution of topography-driven regional groundwater flow to fractal stream chemistry: Residence time distribution analysis of Tóth flow. *Geophysical research letters*, 34, L05403. <https://doi.org/10.1029/2006GL029126>
- Ceola, S., Bertuzzo, E., Singer, G., Battin, T., Montanari, A., & Rinaldo, A. (2014). Hydrologic controls on basin scale distribution of benthic invertebrates. *Water Resources Research*, 50, 2903–2920. <https://doi.org/10.1002/2013WR015111>
- Costigan, K., Daniels, M., & Dodds, W. (2015). Fundamental spatial and temporal disconnections in the hydrology of an intermittent prairie headwater network. *Journal of Hydrology*, 522, 305–316. <https://doi.org/10.1016/j.jhydrol.2014.12.031>
- Costigan, K., Jaeger, K., Goss, C., Fritz, K., & Goebel, P. (2016). Understanding controls on flow permanence in intermittent rivers to aid ecological research: Integrating meteorology, geology and land cover. *Ecology*, 9, 1141–1153. <https://doi.org/10.1002/eco.1712>
- Datry, T., Fritz, K., & Leigh, C. (2016). Challenges, developments and perspectives in intermittent river ecology. *Freshwater Biology*, 61, 1171–1180. <https://doi.org/10.1111/fwb.12789>
- Datry, T., Larned, S. T., & Tockner, K. (2014). Intermittent rivers: A challenge for freshwater ecology. *Bioscience*, 229–235. <https://doi.org/10.1093/biosci/bit027>
- Datry, T., Pella, H., Leigh, C., Bonada, N., & Huguely, B. (2016). A landscape approach to advance intermittency river ecology. *Freshwater Biology*, 61, 1200–1213. <https://doi.org/10.1111/fwb.12645>
- Day, D. (1978). Drainage density changes during rainfall. *Earth Surface Processes*, 3, 319–326.
- Dick, J., Tetzlaff, D., Birkel, C., & Soulsby, C. (2014). Modelling landscape controls on dissolved organic carbon sources and fluxes to streams. *Biogeochemistry*, 122(2-3), 361–374.



- Doering, M., Uehlinger, U., Rotach, A., Schlaepfer, D., & Tockner, K. (2007). Ecosystem expansion and contraction dynamics along a large Alpine alluvial corridor (Tagliamento River, Northeast Italy). *Earth Surface Processes and Landforms*, 32, 1693–1704. <https://doi.org/10.1002/esp.1594>
- Dupas, R., Abbott, B., Minaudo, C., & Fovet, O. (2019). Distribution of landscape units within catchments influences nutrient export dynamics. *Frontiers in Environmental Science*, 7, 43. <https://doi.org/10.3389/fenvs.2019.00043>
- Durighetto, N., Vingiani, F., Bertassello, L., M., Camporese, & Botter, G. (2019). Intra-seasonal drainage network dynamics in a headwater catchment of the Italian Alps [data set]. Retrieved from <http://researchdata.cab.unipd.it/id/eprint/295> doi: <https://doi.org/10.25430/RESEARCHDATA.CAB.UNIPD.IT.00000295>
- Ensign, S., & Martin, W. (2006). Nutrient spiraling in streams and river networks. *Journal of Geophysical Research*, 111, G04009. <https://doi.org/10.1029/2005JG000114>
- Fasching, C., Ulseth, A., Schelker, J., Steniczka, G., & Battin, T. (2016). Hydrology controls dissolved organic matter export and composition in an Alpine stream and its hyporheic zone. *Limnology and oceanography*, 61(2), 558–571. <https://doi.org/10.1002/lno.10232>
- Floriancic, M., van Meerveld, I., Smoorenburg, M., Margreth, M., Naef, F., Kirchner, J., & Molnar, P. (2018). Spatio-temporal variability in contributions to low flows in the high Alpine Poschiavino catchment. *Hydrological processes*, 32, 3938–3953. <https://doi.org/10.1002/hyp.13302>
- Gatto, M., Mari, L., Bertuzzo, E., Casagrandi, R., Righetto, L., Rodriguez-Iturbe, I., & Rinaldo, A. (2013). Generalized reproduction numbers and the prediction of patterns in waterborne disease. *Proceedings of the National Academy of Sciences of the United States of America*, 109, 19,703–19,708. <https://doi.org/10.1073/pnas.1217567109>
- Godsey, S., & Kirchner, J. (2014). Dynamic, discontinuous stream networks: Hydrologically driven variations in active drainage density, flowing channels and stream order. *Hydrological Processes*, 28, 5791–5803. <https://doi.org/10.1002/hyp.10310>
- Goulsbra, C., Evans, M., & Lindsay, J. (2014). Temporary streams in a peatland catchment: Pattern, timing, and controls on stream network expansion and contraction. *Earth Surface Processes and Landforms*, 39(6), 790–803. <https://doi.org/10.1002/esp.3533>
- Gregory, K., & Gardiner, V. (1979). Comment on drainage density and streamflow: A closer look by S. L. Dingman. *Water Resources Research*, 15(6), 1662–1664.
- Gregory, K., & Walling, D. (1968). The variation of drainage density within a catchment. *International Association of Scientific Hydrology Bulletin*, 13, 61–68.
- Helton, A., Hall, R., & Bertuzzo, E. (2017). How network structure can affect nitrogen removal by streams. *Freshwater Biology*, 63, 128–140. <https://doi.org/10.1111/fwb.12990>
- Hewlett, J., & Nutter, W. (1970). The varying source area of streamflow from upland basins, *Symposium on Interdisciplinary Aspects of Watershed Management* pp. 65–83). New York: ASCE.
- Jaeger, K., Montgomery, D., & Bolton, S. (2007). Channel and perennial flow initiation in headwater streams: management implications of variability in source-area size. *Environmental Management*, 40, 775–786. <https://doi.org/10.1007/s00267-005-0311-2>
- Jaeger, K., Sando, R., McShane, R., Dunham, J., Hockman-Wert, D., Kaiser, K., et al. (2019). Probability of streamflow permanence model (PROSPER): A spatially continuous model of annual streamflow permanence throughout the Pacific Northwest. *Journal of Hydrology X*, 2, 100,005. <https://doi.org/10.1016/j.hydroa.2018.100005>
- Jensen, C., McGuide, K., Shao, Y., & Dolloff, C. (2018). Modeling wet headwater stream networks across multiple flow conditions in the Appalachian Highlands. *Earth Surface Processes and Landforms*, 43, 2762–2778. <https://doi.org/10.1002/esp.4431>
- Jensen, C., McGuire, K., McLaughlin, D., & Scott, D. (2019). Quantifying spatiotemporal variation in headwater stream length using flow intermittency sensors. *Environmental Monitoring and Assessment*, 191(4), 226. <https://doi.org/10.1007/s10661-019-7373-8>
- Jensen, C., McGuire, K., & Prince, P. (2017). Headwater stream length dynamics across four physiographic provinces of the Appalachian Highlands. *Hydrological Processes*, 31, 3350–3363. <https://doi.org/10.1002/hyp.11259>
- Kirchner, J. (2009). Catchments as simple dynamical systems: catchment characterization, rainfall-runoff modeling, and doing hydrology backward. *Water Resources Research*, 45, W02429. <https://doi.org/10.1029/2008WR006691>
- Krause, S., Lewandowski, J., Grimm, N., Hannah, D., Pinay, G., & McDonald, K. (2017). Ecohydrological interfaces as hot spots of ecosystem processes. *Water Resources Research*, 53, 6359–6376. <https://doi.org/10.1002/2016WR019516>
- Lazzaro, G., Basso, S., Schirmer, M., & Botter, G. (2013). Water management strategies for run-of-river power plants: Profitability and hydrologic impact between the intake and the outflow. *Water Resources Research*, 49, 8285–8298. <https://doi.org/10.1002/2013WR014210>
- Lovill, S., Hahm, W., & Dietrich, W. (2018). Drainage in the critical zone: Lithologic controls on the persistence and spatial extent of wetted channels during the summer dry season. *Water Resources Research*, 54, 5702–5726. <https://doi.org/10.1029/2017WR021903>
- Malard, F., Uehlinger, U., Zah, R., & Tockner, K. (2006). Flood-pulse and riverscape dynamics in a braided glacial river. *Ecology*, 87(3), 704–716.
- Medici, C., Butturini, A., Bernal, S., Vázquez, E., Sabater, F., Vélez, J., & Francés, F. (2008). Modelling the non-linear hydrological behaviour of a small Mediterranean forested catchment. *Hydrological Processes*, 22, 3814–3828. <https://doi.org/10.1002/hyp.6991>
- Morgan, R. (1972). Observations on factors affecting the behaviour of a first-order stream. *Transactions of the Institute of British Geographers*, 56, 171–185.
- Muneepeerakul, R., Bertuzzo, E., Lynch, J., Fagan, W., Rinaldo, A., & Rodríguez-Iturbe, I. (2008). Neutral metacommunity models predict fish diversity patterns in Mississippi-Missouri basins. *Nature*, 453, 220–222. <https://doi.org/10.1038/nature06813>
- Nicotina, L., Alessi Celegon, E., Rinaldo, A., & Marani, M. (2008). On the impact of rainfall patterns on the hydrologic response. *Water Resources Research*, 44, W12401. <https://doi.org/10.1029/2007WR006654>
- Ocallaghan, J., & Mark, D. (1984). The extraction of drainage networks from digital elevation data. *Computer Vision, Graphics, and Image Processing*, 28(3), 323–344. [https://doi.org/10.1016/S0734-189X\(84\)80011-0](https://doi.org/10.1016/S0734-189X(84)80011-0)
- Ovenden, J., & Gregory, K. (1980). The permanence of stream networks in Britain. *Earth Surface Processes*, 5, 47–60.
- Peirce, S., & Lindsay, J. (2015). Characterizing ephemeral streams in a southern Ontario watershed using electrical resistance sensors. *Hydrological Processes*, 29, 103–111. <https://doi.org/10.1002/hyp.10136>
- Prancevic, J., & Kirchner, J. (2019). Topographic controls on the extension and retraction of flowing streams. *Geophysical Research Letters*, 46, 2084–2092. <https://doi.org/10.1029/2018GL081799>
- Raymond, P., Hartmann, J., Lauerwald, R., Sobek, S., McDonald, C., Hoover, M., et al. (2013). Global carbon dioxide emissions from inland waters. *Nature*, 503, 355–360. <https://doi.org/10.1038/nature12760>
- Roberts, M. (1978). Variation of drainage density in a small British Columbia watershed. *AWRA Water Resources Bulletin*, 14(2), 470–476.
- Roberts, M., & Klingeman, P. (1972). The relationship between drainage net fluctuation and discharge. In Adams, & Helleiner (Eds.), *International Geography, Proceedings of the 22nd International Geographical Congress* (pp. 189–191). Canada: University of Toronto Press.
- Rodríguez-Iturbe, I., González-Sanabria, M., & Bras, R. (1982). A geomorphoclimatic theory of the instantaneous unit hydrograph. *Water Resources Research*, 18(4), 877–886. <https://doi.org/10.1029/WR018i004p00877>

- Settin, T., Botter, G., Rodriguez-Iturbe, I., & Rinaldo, A. (2007). Numerical studies on soil moisture distributions in heterogeneous catchments. *Water Resources Research*, 43, W05425. <https://doi.org/10.1029/2006WR005737>
- Shaw, S. (2016). Investigating the linkage between streamflow recession rates and channel network contraction in a mesoscale catchment in New York state. *Hydrological Processes*, 30, 479–492. <https://doi.org/10.1002/hyp.10626>
- Shaw, S., Bonville, D., & Chandler, D. (2017). Combining observations of channel network contraction and spatial discharge variation to inform spatial controls on baseflow in Birch Creek, Catskill Mountains, USA. *Journal of Hydrology: Regional Studies*, 12, 1–12. <https://doi.org/10.1016/j.ejrh.2017.03.003>
- Superior institute for environmental research and protection (ISPRA)—Italian geologic map sheet 11 (2019). Retrieved from [http://193.206.192.231/carta\\_geologica\\_italia/tavoletta.php?foglio=11](http://193.206.192.231/carta_geologica_italia/tavoletta.php?foglio=11)
- Tarboton, D. (1996). Fractal river networks, Horton's laws and Tokunga cyclicity. *Journal of Hydrology*, 187, 105–117. [https://doi.org/10.1016/S0022-1694\(96\)03089-2](https://doi.org/10.1016/S0022-1694(96)03089-2)
- Tischendorf, W. (1969). *Tracing stormflow to varying source areas in a small, forested watershed in the southeastern Piedmont*. Georgia: University of Georgia: Athens.
- Tonkin, J., Altermatt, F., Finn, D., Heino, J., Olden, J., Pauls, S., & Lytle, D. (2017). The role of dispersal in river network metacommunities: Patterns, processes, and pathways. *Freshwater Biology*, 63, 141–163. <https://doi.org/10.1111/fwb.13037>
- van Meerveld, H., Kirchner, J., Vis, M., Assendelft, R., & Seivert, J. (2019). Expansion and contraction of the flowing network changes hillslope flowpath lengths and the shape of the travel time distribution. *Hydrological and Earth System Sciences*, 23, 4825–4834. <https://doi.org/10.5194/hess-2019-218>
- Veneto region environmental protection agency (ARPAV)—Climatic data download page (2019). Retrieved from [https://www.arpa.veneto.it/bollettini/storico/Mappa\\_2019\\_TEMP.htm](https://www.arpa.veneto.it/bollettini/storico/Mappa_2019_TEMP.htm)
- von Schiller, D., Marcé, R., Obrador, B., Gómez-Gener, L., Casas-Ruiz, J., Acuña, V., & Koschorreck, M. (2014). Carbon dioxide emissions from dry watercourses. *Inland Waters*, 4, 377–382. <https://doi.org/10.5268/IW-4.4.746>
- Ward, A., Schmadel, N., & Wondzell, S. (2018). Simulation of dynamic expansion, contraction, and connectivity in a mountain stream network. *Advances in Water Resources*, 114, 64–82. <https://doi.org/10.1016/j.advwatres.2018.01.018>
- Whiting, J., & Godsey, S. (2016). Discontinuous headwater stream networks with stable flowheads, Salmon River basin, Idaho. *Hydrological Processes*, 30, 2305–2316. <https://doi.org/10.1002/hyp.10790>
- Wiginton, P., TJ, M., & DR, L. (2005). Stream network expansion: A riparian water quality factor. *Hydrological Processes*, 19(8), 1715–1721. <https://doi.org/10.1002/hyp.5866>
- Zimmer, M., & McGlynn, B. (2017). Ephemeral and intermittent runoff generation processes in a low relief, highly weathered catchment. *Water Resources Research*, 53, 7055–7077. <https://doi.org/10.1002/2016WR019742>